Geoacoustic inversion using low frequency broadband acoustic measurements from L-shaped arrays in the Shallow Water 2006 Experiment

Lin Wan, Mohsen Badiey and David P. Knobles

Citation: The Journal of the Acoustical Society of America **140**, 2358 (2016); doi: 10.1121/1.4962558
View online: https://doi.org/10.1121/1.4962558
View Table of Contents: https://asa.scitation.org/toc/jas/140/4
Published by the Acoustical Society of America

Geoacoustic inversion using low frequency broadband acoustic measurements from L-shaped arrays in the Shallow Water 2006 Experiment

Lin Wan[a] and Mohsen Badiey
College of Earth, Ocean, and Environment, University of Delaware, Newark, Delaware 19716, USA

David P. Knobles[b]
Knobles Scientific and Analysis, LLC., Austin, Texas 78755, USA

(Received 4 February 2016; revised 12 August 2016; accepted 30 August 2016; published online 6 October 2016)

When using geoacoustic inversion methods, one objective function may not result in a unique solution of the inversion problem because of the ambiguity among the unknown parameters. This paper utilizes acoustic normal mode dispersion curves, mode shapes, and modal-based longitudinal horizontal coherence to define a three-objective optimization problem for geoacoustic parameter estimation. This inversion scheme is applied to long-range combustive sound source data obtained from L-shaped arrays deployed on the New Jersey continental shelf in the summer of 2006. Based on the sub-bottom layering structure from the Compressed High-Intensity Radiated Pulse reflection survey at the experimental site, a two-layer (sand ridge overlaying a half-space basement) range-independent sediment model is utilized. The ambiguities of the sound speed, density, and depth of the sand ridge layer are partially removed by minimizing these objective functions. The inverted seabed sound speed over a frequency range of 15–170 Hz is comparable to the ones from direct measurements and other inversion methods in the same general area. The inverted seabed attenuation shows a nonlinear frequency dependence expressed as $\alpha_b = 0.26f^{1.55}(\mathrm{dB/m})$ from 50 to 500 Hz or $\alpha_b = 0.32f^{1.65}(\mathrm{dB/m})$ from 50 to 250 Hz, where f is in kHz.
 [http://dx.doi.org/10.1121/1.4962558]

[TMS] Pages: 2358–2373

I. INTRODUCTION

Among the acoustic properties of marine sediments, compressional sound speed and attenuation play dominant roles in affecting sound propagation in a shallow water environment. The frequency dependence of these properties is important in the geoacoustic model of ocean sediments, which incorporates the physics of acoustic sediment interaction. Hamilton derived empirical geoacoustic models,[1] suggesting the seabed sound speed can be well described by a sound speed ratio at the surface and a depth gradient, and the attenuation increases linearly with frequency over the full frequency range; however, the existence of seabed sound speed dispersion and nonlinear frequency dependence of seabed attenuation in sandy bottoms at low frequency are predicted by other seabed geoacoustic models, such as the Biot-Stoll poro-elastic model.[2–5] Therefore, experimental databases of low frequency seabed sound speed and attenuation are desirable to test the validity of the geoacoustic models. At low frequencies, it is difficult to make a direct measurement of the attenuation. Thus, inversion methods based on acoustic field measurements are helpful for effectively estimating the low frequency seabed sound speed and attenuation. When low-frequency sound is transmitted into the sea floor, its energy loss is due to many mechanisms, including the intrinsic attenuation caused by conversion of energy into heat, sound scattering by inhomogeneities within the sediment and its boundaries, and other mechanisms.[1] When "attenuation" is used in this paper, it refers to the energy loss through all these mechanisms rather than intrinsic attenuation. Thus, it is "effective attenuation." For the purposes of sonar performance prediction, effective attenuation could be adequate to calculate the low-frequency long-range shallow water acoustic field. The goals of this paper are to (1) propose a three-objective geoacoustic inversion scheme based on normal mode dispersion curves, mode shapes, and modal-based longitudinal horizontal correlation coefficients; (2) analyze modal dispersion, mode shapes, and longitudinal horizontal coherence of broadband combustive sound source (CSS) signals obtained by L-shaped arrays in the Shallow Water 2006 (SW06) Experiment; and (3) study the correlations of parameters and invert them using results from the first and second goals.

SW06 was a large acoustic experiment conducted on the New Jersey continental shelf in the summer of 2006.[6] Over its two-month duration, a number of sub-experiments were conducted to estimate the geoacoustic parameters as a function of frequency. Knobles *et al.*[7] inverted the bottom sound speed using the arrival structure of acoustic broadband signals, and then obtained the bottom attenuation from long-range transmission loss (TL) data. Jiang *et al.*[8,9] used the short-range travel time measurements to estimate the bottom sound speed and inferred the frequency dependence of the attenuation by comparing the amplitude ratio of the reflections from the sea bottom and a sub-bottom sediment layer.

[a]Electronic mail: wan@udel.edu
[b]Also at: College of Earth, Ocean, and Environment, University of Delaware, Newark, DE, 19716.

Choi *et al.*[10] obtained the seabed sound speed and attenuation from travel time difference and reflection coefficient measurement, respectively.

In order to obtain the solution of the geoacoustic inversion problem, one needs to consider the correlation between various parameters. For example, the geoacoustic inversion method using TL to define an objective function may not result in a unique solution because of the ambiguity between seabed sound speed and attenuation. Since there is more than one pair of seabed sound speed and attenuation parameter values yielding the desired minimum of the objective function, additional constraints from other inversion methods or the knowledge from direct measurements are required to successfully invert the sound speed and attenuation.

Different characteristics of the normal modes have been successfully utilized in determining the geoacoustic parameters. The inversion methods using modal dispersion,[11–13] modal attenuation,[11,14] modal amplitude ratio,[11,15,16] modal depth function,[17,18] and modal-based vertical coherence[19] have been summarized and discussed by Zhou *et al.*[20] These normal mode characteristics can be utilized to define multi-objective optimization problems for geoacoustic parameter estimation. In this paper, a three-objective geoacoustic inversion scheme based on a normal mode method is developed. The dispersion characteristics of normal modes are used to define the first objective function, which calculates the difference between the modeled and measured modal arrival times for different modes and frequencies. A hybrid optimization method, including a genetic algorithm (GA)[21] and a pattern search algorithm,[22] is utilized to find the global minimum of the first objective function and to estimate the seabed parameters and their correlations. The second objective function calculates the difference between the modeled and measured mode shapes. The inverted results from the first objective function are then used as constraints in the minimization of the second objective function to partially remove ambiguities of sound speed and density of the surface sand layer. The theoretical longitudinal horizontal coherence derived in terms of normal modes is utilized to compare with the measured results for constructing the third objective function. By minimizing the third objective function, the seabed sound attenuation as a function of frequency can be estimated.

The remainder of this paper is organized as follows. Section II describes the experimental setup of one sub-experiment in SW06. Section III presents the estimation of seabed parameters using modal dispersion curves. The ambiguity of sound speed, density, and depth of the surface sand layer is also discussed. Section IV shows removal of the aforementioned ambiguity by data-model comparison of acoustic normal mode shapes. Section V shows the estimation of seabed sound attenuation using longitudinal horizontal coherence of the received acoustic field. Section VI presents the comparison with other results. Finally, Sec. VII contains the summary and conclusion.

II. EXPERIMENTAL DESCRIPTION

During SW06, one 32-element L-shaped array named Shallow Water Acoustic Measurement Instrumentation (SWAMI 32) and one 52-element L-shaped array named Shallow Water Acoustic Measurement Instrumentation (SWAMI 52) were deployed about 20 km apart at site A (39° 3.6180′ N, 73° 7.8970′ W) and site B (39° 12.0010′ N, 72° 57.9740′ W), respectively [Fig. 1(a)]. The water depth (D_1) along AB was about 72.7 ± 1.9 m (Knudsen echo sounder, 12 kHz). The vertical line array (VLA) portions of both SWAMI 32 and SWAMI 52 covered most of the water column. The horizontal line array (HLA) portions of SWAMI 32 and SWAMI 52 had 20 elements and 36 elements, respectively, and were positioned on the sea bottom. The sampling frequencies for SWAMI 32 and SWAMI 52 were 6250 and 2400 Hz, respectively. The high pass filter cut was 2 Hz. The HLA portion (channels 13–32) of SWAMI 32 had a length of 256.43 m. The spacing between subsequent HLA elements decreased along the SWAMI 32 HLA. The element spacing of SWAMI 32 is shown in the top four rows of Table I. The hydrophones corresponding to channels 13 and 32 of SWAMI 32 were located at (39° 3.615′ N, 73° 7.9008′ W) and (39° 3.5160′ N, 73° 8.0240′ W), respectively. The array bearing of the SWAMI 32 HLA was 224°. The length of the HLA portion (channels 17–52) of SWAMI 52 was 230 m. Its element spacing can be found in the bottom eight rows of Table I. The array bearing of the SWAMI 52 HLA was 314°, which is perpendicular to the HLA of SWAMI 32. From August 29, 2006 to September 4, 2006, several CSSs were deployed at different distances between the source ship (R/V Knorr) and the two L-shaped arrays.

The CSS generation system, used in the experiment, can produce high intensity, low frequency acoustic pulses by igniting a combustible gas mixture captured in a combustion chamber.[23] The source ship traveled along the line connecting A and B. The track AB is along the continental shelf. The sound propagation direction was perpendicular to the HLA portion of SWAMI 52 and parallel to the HLA portion of SWAMI 32 [Fig. 1(b)]. This experimental configuration offered an opportunity to obtain the modal dispersion curves, mode shapes, and longitudinal horizontal coherence for geoacoustic inversion.

Water column sound speed profiles (SSP) were determined from the source ship conductivity-temperature-depth (CTD) data. The left panel of Fig. 2 shows the average sound speed profile measured on September 4, 2006. The average measured sound speed profile is a typical example of downward refraction conditions in a shallow water waveguide.

The approximate sub-bottom layering structure along the straight line AB is obtained from interpolation of the Compressed High-Intensity Radiated Pulse (CHIRP) reflection survey.[7] Track AB is in the middle of a sand ridge,[24] with a depth (D_2) varying between 1 and 4 m over the acoustic track AB.[25] This paper utilizes a two-layer (sand ridge overlaying a half-space basement), range-independent sediment model for inversion. In the right panel of Fig. 2, red circles indicate the hydrophone elements of SWAMI 32 and SWAMI 52; D_1 and D_2 are the water depth and the layer depth of the sand ridge, respectively; c_1 and c_2 are sound speeds in the sand ridge and the half-space basement, respectively; ρ_1 and ρ_2 are densities of the two layers, respectively. The experimental data used in this paper were obtained from

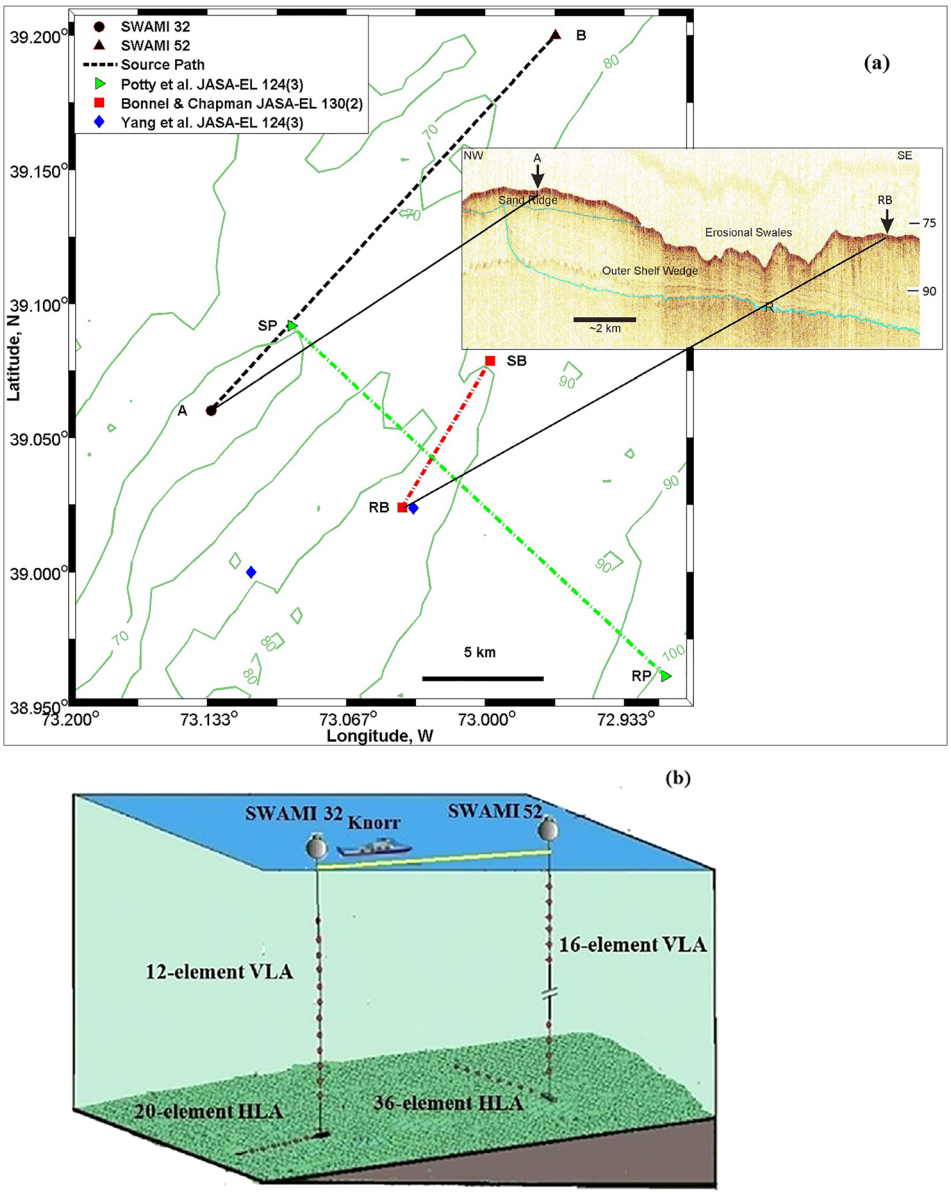

FIG. 1. (Color online) Experimental configuration. (a) Top view. The inset figure from Ref. 7 shows the sub-bottom chirp reflection profile of the seabed perpendicular to bathymetry isobaths. (b) 3D view.

long-range sound propagation, which is dominated by the surficial seafloor with a thickness on the order of a few wavelengths. There is little difference in the attenuation in the top few tens of meters in the bottom.[1] Therefore, the sound attenuation in the seabed (α_b) is assumed to be the same in both layers. Goff *et al.*[26] reported the average mean grain size distribution of the sand ridge to be 1.3 ϕ between SWAMI 32 and SWAMI 52. Based on the Hamilton semi-

TABLE I. The element spacing of the SWAMI 32 HLA and SWAMI 52 HLA (m).

No.	13	14	15	16	17	18	19	20	21	22
Spacing from 13	0	20.32	39.66	58.06	75.57	92.24	108.10	123.20	137.57	151.24
No.	23	24	25	26	27	28	29	30	31	32
Spacing from 13	164.25	176.63	188.42	199.64	210.31	220.47	230.14	239.34	248.10	256.43
No.	17	18	19	20	21	22	23	24	25	26
Spacing from 17	0	15.84	29.48	41.21	51.32	60.00	67.49	73.94	79.48	84.60
No.	27	28	29	30	31	32	33	34	35	36
Spacing from 17	89.33	93.70	97.74	101.47	104.91	108.09	111.03	113.75	116.25	118.97
No.	37	38	39	40	41	42	43	44	45	46
Spacing from 17	121.91	125.09	128.53	132.26	136.30	140.67	145.40	150.52	156.07	162.51
No.	47	48	49	50	51	52				
Spacing from 17	169.99	178.69	188.79	200.52	214.16	230.00				

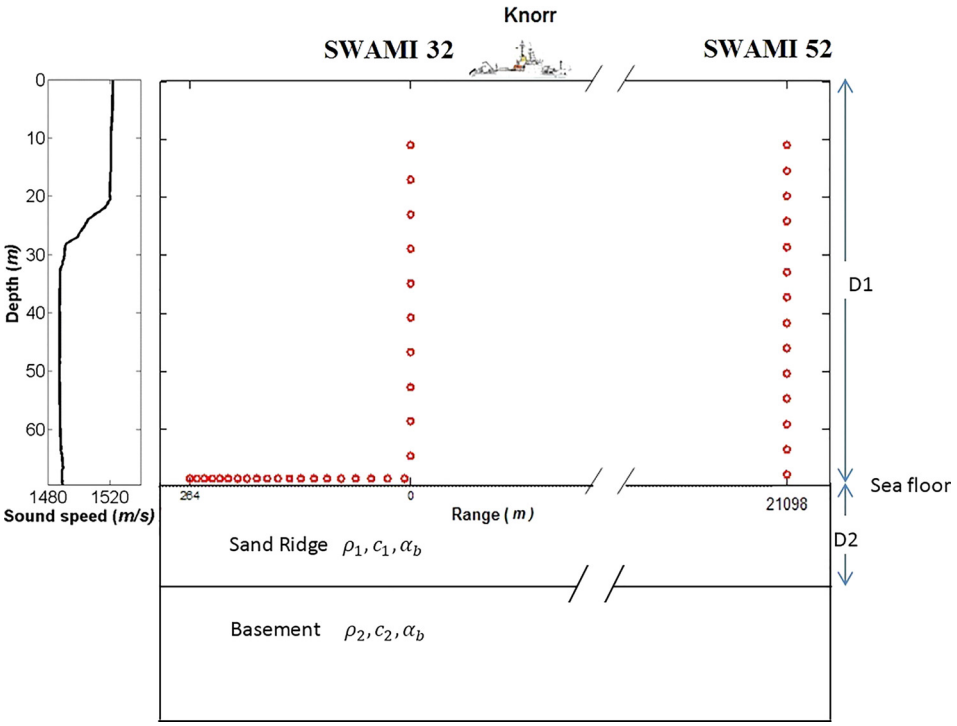

FIG. 2. (Color online) Measured water column sound speed profile and two-layer seabed used in geoacoustic inversion.

empirical geoacoustical model,[1] this description corresponds to a coarse sand. Yang *et al.*[27] used the sediment acoustic-speed measurement system to directly measure the seabed sound speed in the frequency range 2–35 kHz at three locations in the SW06 area shown by diamonds in Fig. 1(a). It is noted that these direct measurements were made in an area where the sediment layer was a mixture of sand and clay unlike the sand ridge. The maximum penetration of the measurement device was 3 m. The depth-averaged seabed sound speed reported by this direct measurement was between 1588 and 1622 m/s.

III. GEOACOUSTIC INVERSION FROM MODAL ARRIVAL TIME DIFFERENCE

In this section, the dispersion characteristics of acoustic normal modes are applied in the estimation of seabed parameters. The modal arrival time differences are utilized to define the objective function, which is the difference between the modeled and measured modal arrival times. Section III A describes the calculation of modal arrival time difference for different modes and frequencies. Section III B shows the extraction of modal arrival time difference from experimental data. The inversion scheme and inverted results using the modal arrival time difference method are presented in Sec. III C.

A. The mathematical expression for modal arrival time difference

When a broadband signal propagates in shallow water, its group velocities differ for different frequencies and modes. The group velocity V_g^n of the nth mode satisfies[20,28]

$$\frac{1}{V_g^n} = \frac{2\pi f}{k_n N_n}\int_0^\infty \frac{\rho(z)}{c^2(z)}|\Psi_n(z,f)|^2 dz, \tag{1}$$

where Ψ_n is the frequency-dependent mode depth function of the nth mode, k_n is the horizontal wave number eigenvalue of the nth mode, N_n is the normalization factor of the nth mode, ρ is the density, and c is the sound speed.

The following is used in a two-layer bottom model:

$$\begin{aligned}\int_0^\infty \frac{\rho(z)}{c^2(z)}|\Psi_n(z,f)|^2 dz = &\int_0^{D1} \frac{\rho_0}{c_0{}^2(z)}|\Psi_n(z,f)|^2 dz \\ &+ \int_{D1}^{D1+D2} \frac{\rho_1}{c_1{}^2}|\Psi_n(z,f)|^2 dz \\ &+ \int_{D1+D2}^{\infty} \frac{\rho_2}{c_2{}^2}|\Psi_n(z,f)|^2 dz, \end{aligned}\tag{2}$$

where c_0 is the sound speed in the water column, D_1 is the water depth, and D_2 is the depth of the sand ridge.

The arrival time difference between two frequencies (f_H and f_L) for the nth mode at range r can be expressed by

$$\begin{aligned}\Delta T_n(f_H,f_L) = \frac{2\pi r}{k_n N_n}\Bigg(&f_H\int_0^\infty \frac{\rho(z)}{c^2(z)}|\Psi_n(z,f_H)|^2 dz \\ &- f_L\int_0^\infty \frac{\rho(z)}{c^2(z)}|\Psi_n(z,f_L)|^2 dz\Bigg).\end{aligned}\tag{3}$$

The arrival time difference between two modes (m and n) for the same frequency f at range r is given by

$$\begin{aligned}\Delta T_{nm}(f) = 2\pi f r\Bigg(&\frac{1}{k_m N_m}\int_0^\infty \frac{\rho(z)}{c^2(z)}|\Psi_m(z,f)|^2 dz \\ &- \frac{1}{k_n N_n}\int_0^\infty \frac{\rho(z)}{c^2(z)}|\Psi_n(z,f)|^2 dz\Bigg).\end{aligned}\tag{4}$$

Using a normal mode code, such as KRAKEN,[29] the modal arrival time differences, $\Delta T_n(f_H,f_L)$ and $\Delta T_{nm}(f)$, can be calculated.

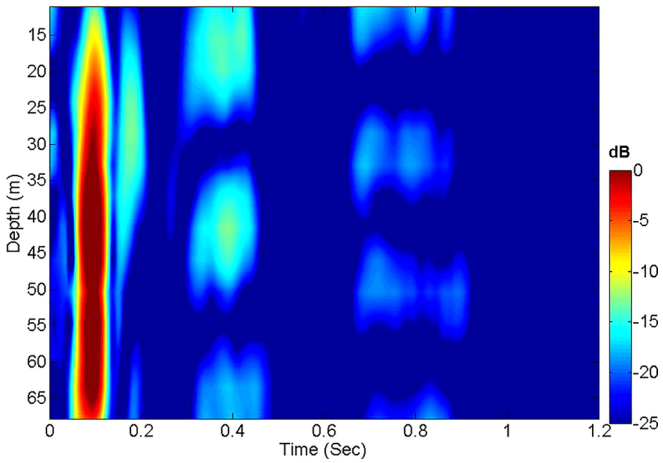

FIG. 3. (Color online) Received acoustic intensity (dB relative to the maximum value) from 16 hydrophones of the SWAMI 52 VLA at a range of 16.33 km.

B. The experimental modal arrival time difference measurements

The acoustic normal modes can be identified using the CSS signal from long-range sound propagation. The received acoustic intensity (dB relative to the maximum value) of the VLA portion of SWAMI 52, at a range of 16.33 km when the CSS depth is 50 m, is shown in Fig. 3. The received signal is filtered by a one-third octave bandpass filter with a center frequency of 100 Hz. The first four modes can be identified around 0.1, 0.18, 0.39, and 0.78 s, respectively. For a given distance, the intensity of each mode depends on the mode depth function and the source depth (SD). Mode 2 has one node below 45 m. Mode 3 has two nodes, which are close to 30 and 55 m, respectively. The three nodes of mode 4 are located at depths of 20, 40, and 60 m, respectively. In this paper, the arrival time of each mode is identified by using the peak of its amplitude. Then, the measured modal arrival time is obtained by averaging the modal arrival times over 36 hydrophones of the SWAMI 52 HLA, which is perpendicular to the direction of sound propagation.

The received broadband acoustic signal can be processed using the wavelet scalogram,[12] adaptive optimal-kernel based time-frequency representation (AOK-TFR),[13,18] and warping operators[30] to obtain the experimental group velocity dispersion curves. Figure 4(a) shows the AOK-TFR of the measured time series from a single hydrophone (# 17) of the SWAMI 52 HLA at a distance of 16.33 km when the SD is 50 m; Fig. 4(b) shows the AOK-TFR of the measured time series averaged over 36 hydrophones of the SWAMI 52 HLA. The comparison of Figs. 4(a) and 4(b) appears to show that the signal-to-noise ratio (SNR) is increased by averaging out the random noise in a single hydrophone. In Fig. 4(a), the noise appears as four "horizontal stripes" at <5, ~75, ~125, and ~175 Hz. In Fig. 4(b), this type of noise has been reduced. The dispersion curves of the first five modes shown in Fig. 4(b) can be more easily identified. The experimental arrival time differences ($\Delta T'_n$ and $\Delta T'_{nm}$) corresponding to the first five modes and frequencies from 15 to 170 Hz are extracted from Fig. 4(b) and listed in Table II.

C. Inversion scheme and results using modal arrival time difference

In Eqs. (2), (3), and (4), both $\Delta T_n(f_H, f_L)$ and $\Delta T_{nm}(f)$ depend on the sound speeds (c_1 and c_2), densities (ρ_1 and ρ_2), water depth (D_1), and the depth of sand ridge layer (D_2). Therefore, values for the six unknown parameters (c_1, c_2, ρ_1, ρ_2, D_1, and D_2) can be estimated by matching the calculated group velocity dispersion curves [$\Delta T_n(f_H, f_L)$ and $\Delta T_{nm}(f)$] with the experimental data ($\Delta \hat{T}_n$ and $\Delta \hat{T}_{nm}$). The objective function is defined by

$$E_1(\mathbf{x}) = \sum_f \left(\sum_n \left(\Delta T_n(f,\mathbf{x}) - \Delta \hat{T}_n(f)\right)^2 + \sum_{m,n(m\neq n)} \left(\Delta T_{nm}(f,\mathbf{x}) - \Delta \hat{T}_{nm}(f)\right)^2 \right), \quad (5)$$

where $\mathbf{x} = [c_1, c_2, \rho_1, \rho_2, D_1, D_2]$.

Both local and global optimization methods have been successfully applied to find the minimum of an objective function in a geoacoustic inversion approach. Gerstoft applied a combination of GAs and the Gauss-Newton

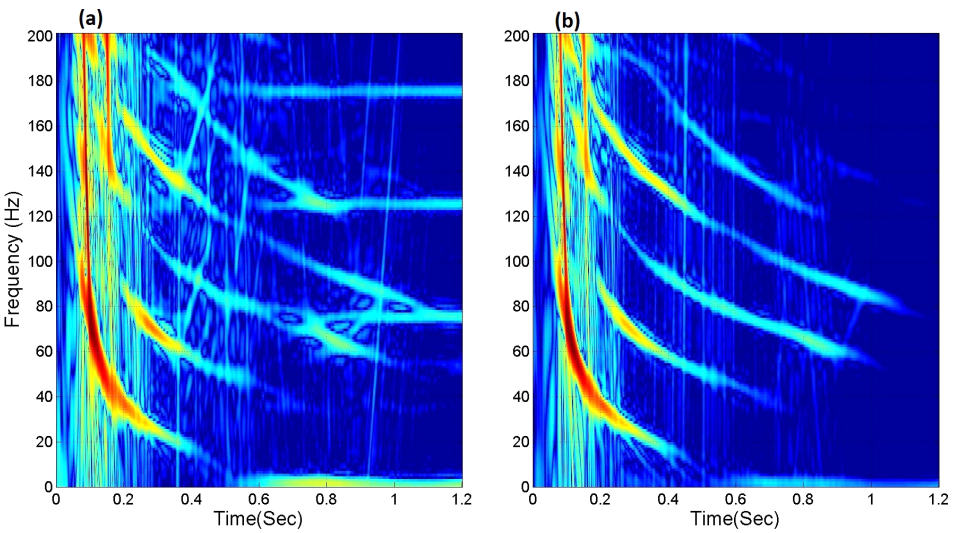

FIG. 4. (Color online) AOK-TFR of the measured CSS signal: (a) from a single hydrophone (#17) of the SWAMI 52 HLA and (b) from 36 hydrophones of the SWAMI 52 HLA.

TABLE II. Extracted modal arrival time differences.

f (Hz)		50	70	75	90	105	135	160		
$\Delta T'_{12}$(s)		0.386	0.181							
$\Delta T'_{23}$(s)			0.457	0.380	0.237					
$\Delta T'_{34}$(s)					0.483	0.367	0.188			
$\Delta T'_{45}$(s)							0.315	0.251		
f_H (Hz)	18	20	50	70	75	90	105	135	160	170
$\Delta T'_1$(s) ($f_L = 15$ Hz)	0.027	0.050	0.264	0.301						
$\Delta T'_2$(s) ($f_L = 40$ Hz)			0.160	0.402	0.430	0.490				
$\Delta T'_3$(s) ($f_L = 60$ Hz)				0.175	0.280	0.483	0.607	0.743		
$\Delta T'_4$(s) ($f_L = 80$ Hz)						0.148	0.388	0.703	0.845	0.886
$\Delta T'_5$(s) ($f_L = 115$ Hz)								0.245	0.451	

approach to geoacoustic inversion.[31] Potty *et al.*[12] used a hybrid scheme in the inversion for sediment compressional wave velocity, where the best parameter vector obtained by a GA search is further optimized using the Levenberg-Marquardt algorithm. In this paper, a hybrid optimization algorithm, which includes a GA and a pattern search algorithm,[22] is utilized to find the global minimum of the objective function. The optimum parameters obtained from the GA inversion are used as a starting point for the pattern search algorithm. The pattern search algorithm searches for a set of points forming a mesh around the current point. The mesh is formed by adding the current point to a scalar multiple of a fixed set of vectors called a *pattern*. Through a set of steps, the pattern search algorithm computes a sequence of points that migrate to the optimal point, which corresponds to the minimum of the objective function or the inversion solution.

The estimation process using this hybrid optimization algorithm is shown as Step 1 in Fig. 5. It is noted that the seabed attenuation (α_b) is not considered as a parameter to be inverted in this first step. Because the group velocity does not depend on the seabed attenuation as shown in Eq. (1), an estimate for its values cannot be obtained in Step 1.

The KRAKEN algorithm calculated the modal arrival time differences, ΔT_n and ΔT_{nm}, as a function of f, c_1, c_2, ρ_1, ρ_2, D_1, and D_2, using the measured water column SSP and the distance between the CSS deployment position and SWAMI 52. The experimental modal arrival time differences in Table II ($\Delta\hat{T}_n$ and $\Delta\hat{T}_{nm}$) are used as the experimental inputs to the objective function shown as Eq. (5). The value of $E_1(\mathbf{x})$ as a function of each unknown parameter is shown in Fig. 6. The dots show all sampled parameter values used in the GA inversion. The optimum parameters obtained from GA corresponds to the dot with the minimum value of E_1, which is utilized as the starting point (input) for the pattern search algorithm. The optimal output of the pattern search corresponds to the inversion solution. The horizontal coordinate of the vertical red line in each scatter plot represents the inverted result of each unknown parameter obtained by the hybrid optimization scheme. The sound speed in the basement is the most sensitive parameter. By minimizing the objective function, the inverted water depth (D_1) is 70.8 m; the estimated sound speed of the half-space basement (c_2) is 1730.0 m/s; the inverted density of the half-space basement (ρ_2) is 1844.0 kg/m^3. While the environment is range-dependent, these estimates are based on a range-independent model and thus may contain bias and/or uncertainty associated with model error.

The three unknown parameters (c_1, ρ_1, and D_2) cannot be inverted in this step because of their ambiguity shown by the second term on the right side of Eq. (2). For a given arrival time difference, an increase (decrease) in sound speed of the sand ridge (c_1) can be compensated by increasing (decreasing) the density (ρ_1) or layer depth (D_2).

Zhou *et al.*[20] discussed the coupling relationship between seabed sound speed and attenuation in the TL-based geoacoustic inversion method. Inspired by their analysis, we examine the integrand (ρ_1/C_1^2) of the second integral on the right side of Eq. (2) to obtain the coupling relationship between seabed sound speed (c_1) and density (ρ_1) of the sand ridge. The value of E_1 as a function of three unknown parameters (c_1, ρ_1, and D_2) and ρ_1/C_1^2 are shown in Figs. 7(a)–7(d), respectively. The term, ρ_1/C_1^2, reaches the minimum of Eq. (5) at 6.3×10^{-4}(kg s^2/m^5). Using this constraint, the value of E_1 as a function of c_1 and D_2 is shown in Figs. 7(e) and 7(f), respectively. D_2 is estimated to be 1.37 m. In order to mitigate the ambiguity between seabed sound speed (c_1) and density (ρ_1) of the sand ridge, additional constraints or objective functions are required. The mode shape of an acoustical normal mode depends on both seabed sound speed (c_1) and density (ρ_1), thus it is selected to construct the objective function in Sec. IV.

IV. GEOACOUSTIC INVERSION USING MODE SHAPE

The mode shape of an acoustic normal mode has been used to invert for the seabed sound speed in shallow water.[17,18] In this section, the data-model comparison of mode shape is utilized to define the second objective function to remove the ambiguity of sound speed (c_1) and density (ρ_1) in the sand ridge.

A. The mathematical expression for mode shape at the water-seabed interface

The impedance at the water-seabed interface can be expressed by

$$Z_{1,n} = \frac{-\rho_0}{\partial\Psi_n(z)/\partial z}\Psi_n(z)\Big|_{z=D_1} \tag{6}$$

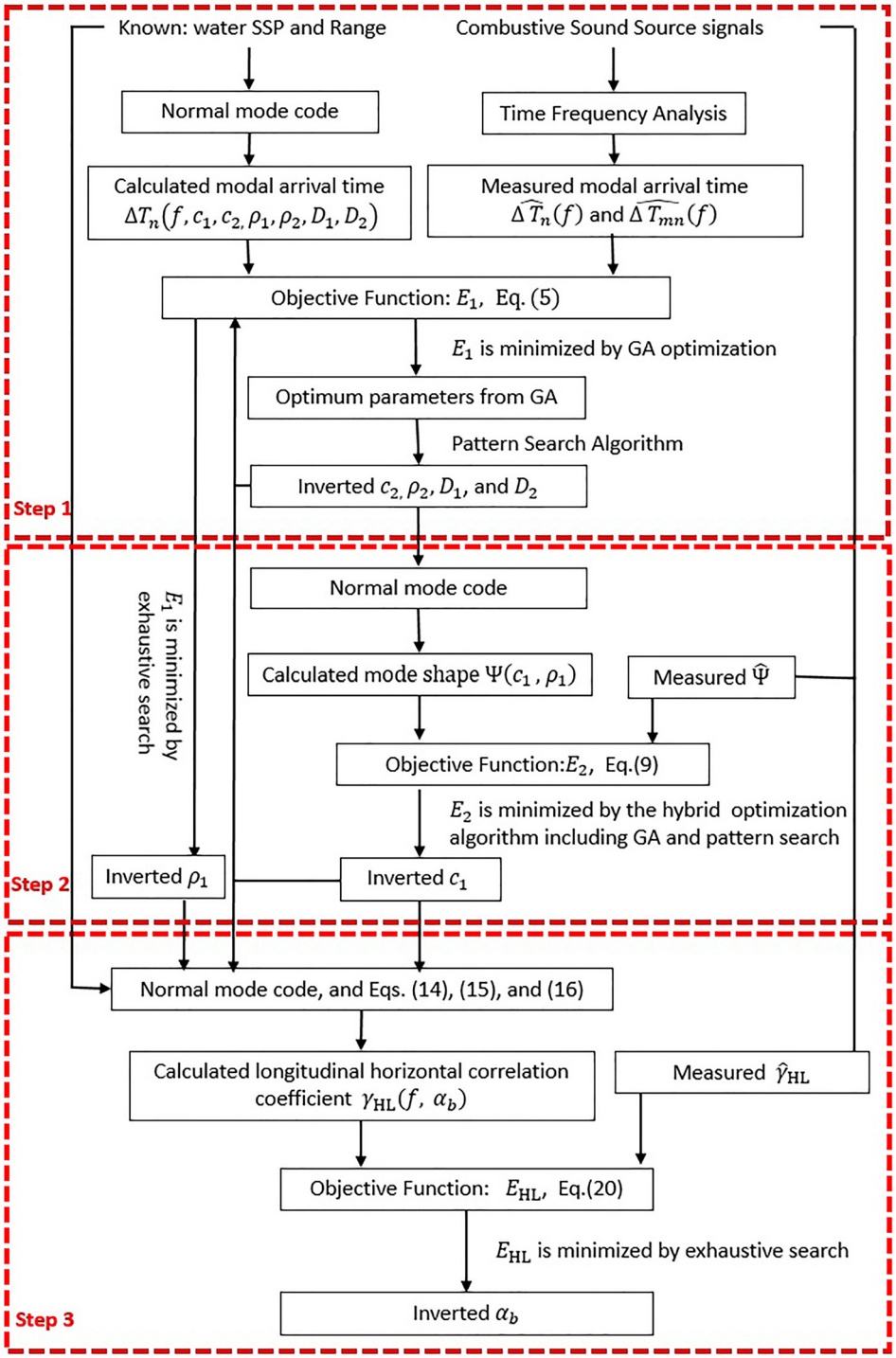

FIG. 5. (Color online) Three-step estimation process.

and

$$Z_{2,n} = \frac{\rho_1}{\sqrt{k_n^2 - (2\pi f/c_1)^2}}, \tag{7}$$

where $Z_{1,n}$ is the impedance calculated from the nth mode shape in water column and $Z_{2,n}$ is the impedance obtained using the parameters in the sand ridge layer.

The boundary condition at the water-sediment interface is satisfied by letting $Z_{1,n} = Z_{2,n}$, where one then obtains

$$\left.\frac{\Psi_n(z)}{\partial\Psi_n(z)/\partial z}\right|_{z=D_1} = \frac{-\rho_1/\rho_0}{\sqrt{k_n^2 - (2\pi f/c_1)^2}}. \tag{8}$$

Equation (8) shows the mode shape is a function of the sound speed (c_1) and density (ρ_1) of the sand ridge layer.

B. The data-derived mode shape

Since the eigenvectors of the cross-spectral density matrix (CSDM) constructed using data from the VLA correspond to the mode shapes, one can extract the data-derived mode shapes using the singular value decomposition of the CSDM. A detailed mathematical derivation of this process can be found in Refs. 17, 18, and 32. One requirement for reliable CSDM-based mode extraction is that the receivers sample the modes sufficiently well in depth. The number of

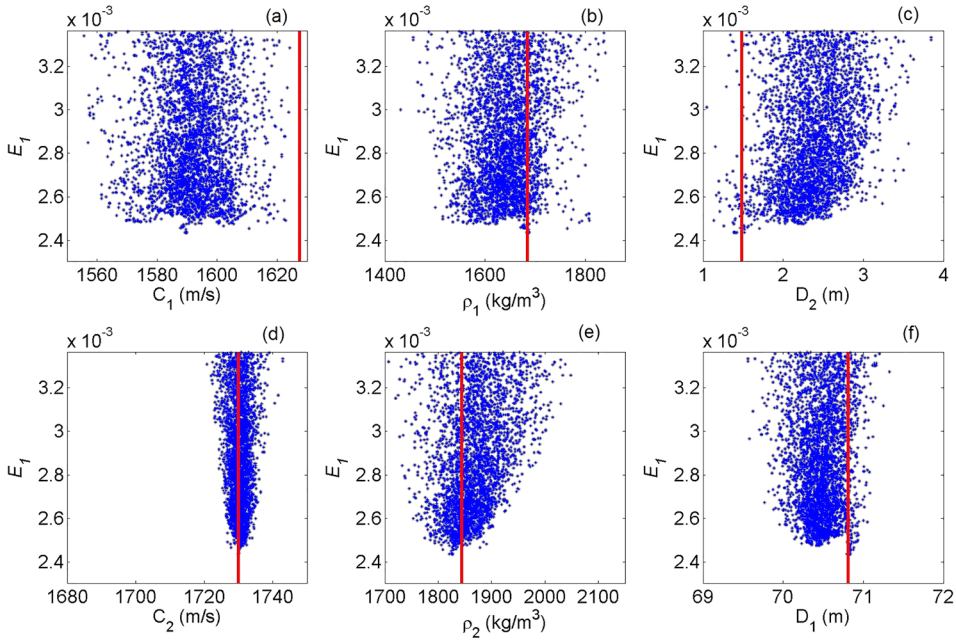

FIG. 6. (Color online) E_1 as a function of (a) sound speed in sand ridge; (b) density in sand ridge; (c) depth of sand ridge; (d) sound speed in the half-space basement; (e) density in the basement; and (f) water depth. The horizontal coordinate of the vertical line represents the inverted results in Step 1.

modes increases with frequency. The higher-order modes at a higher frequency need to be sampled more finely in depth. The higher-order modes obtained using an under-sampled vertical array may alias into the lower-order modes. Therefore, the CSDM-based mode extraction is more reliable for lower-order modes at a low frequency. The other requirement for the CSDM-based method is that a constant number of modes exist in the frequency band for constructing the CSDM. In this paper, the CSS data received by SWAMI 52 at a range of 16.33 km are utilized. The first 14 rows of the CSDM represent the top 14 elements of the VLA, which covered most parts of the water column. The CSDM is constructed by the measured acoustic pressure spectra in an 8 Hz band with the central frequency of 25 Hz. The aforementioned requirements are satisfied, because only mode one exists in this frequency band and it is well sampled in depth. As shown by Eq. (8), the mode shape at the water-seabed interface is directly related to the bottom parameters. Thus, the last row of the CSDM corresponds to the first element of the HLA, which was positioned on the seabed. The extracted mode shape for mode one is shown in Fig. 8 by circles.

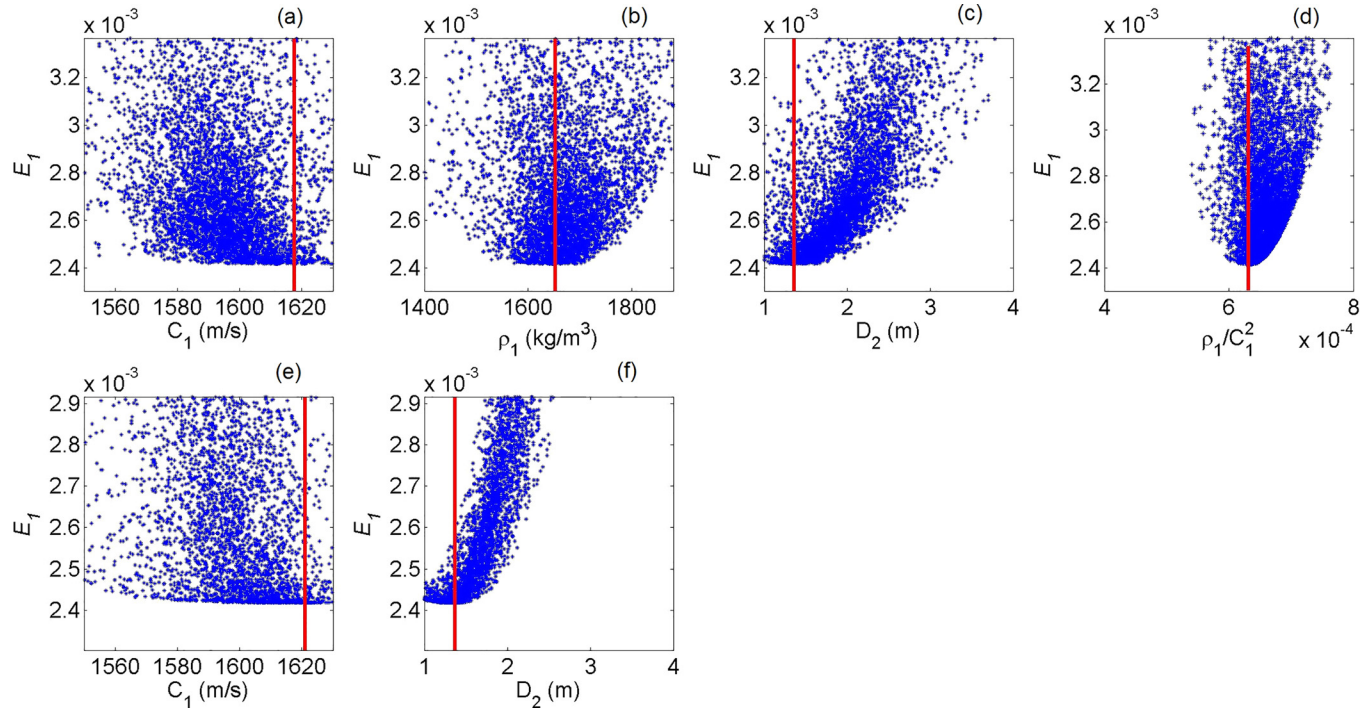

FIG. 7. (Color online) First row: using inverted water depth, sound speed, and density in the basement as constraints, E_1 as a function of (a) sound speed in sand ridge; (b) density in sand ridge; (c) depth of sand ridge; and (d) ρ_1/C_1^2. Second row: E_1 as a function of (e) sound speed in sand ridge and (f) depth of sand ridge after adding the constraint from (d), which is $\rho_1/C_1^2 = 6.3 \times 10^{-4}$ (kg s^2/m^5). The horizontal coordinate of the vertical line represents the inverted results.

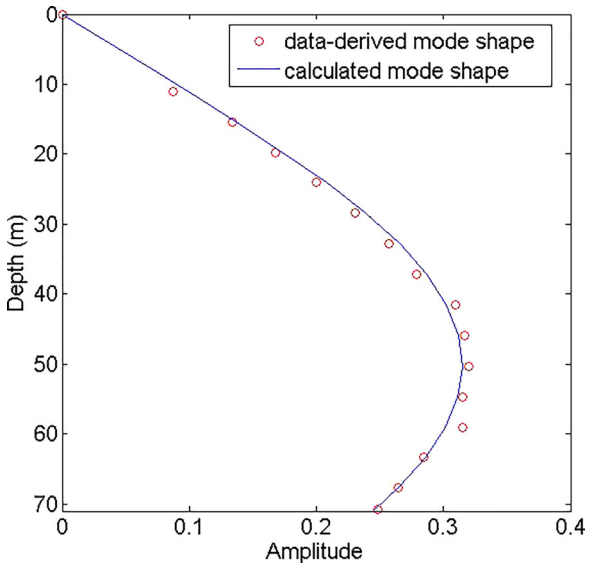

FIG. 8. (Color online) Data-model comparison of the first mode shape at 25 Hz.

C. Inversion scheme and results using mode shape

In this section, the inversion scheme and results based on mode shapes are presented. This scheme is utilized to remove the ambiguity between the sound speed (c_1) and density (ρ_1) in the sand ridge.

Since the mode shape depends on sound speed (c_1) and density (ρ_1) of the sand ridge, as shown in Eq. (8), these two unknown parameters can be estimated by minimizing the difference between modeled and data-derived mode shape. The second objective function of this paper is shown by Eq. (9),

$$E_2(c_1,\rho_1)=\sqrt{\frac{1}{N_{\text{dep}}}\sum_{i=1}^{N_{\text{dep}}}|\hat{\Psi}(z_i)-\Psi(z_i,c_1,\rho_1)|^2}, \qquad (9)$$

where $\hat{\Psi}(z_i)$ is the data-derived mode shape at depth z_i, and N_{dep} is the number of hydrophones employed in the computation.

The estimation process using the hybrid optimization algorithm (GA and the pattern search) is shown as Step 2 in Fig. 5. The calculated mode shape (Ψ), as a function of c_1 and ρ_1, is obtained using the measured water column SSP and the inverted parameters from the first objective function, Eq. (5). The data-derived mode shape ($\hat{\Psi}$) shown in Fig. 8 is used as the experimental inputs to Eq. (9). The value of E_2 as a function of c_1 and ρ_1 is shown in Fig. 9. By minimizing E_2, the estimated sound speed of the sand ridge (c_1) is 1613.3 m/s.

As shown in Fig. 9(b), ρ_1 is not a sensitive parameter for E_2. In order to determine ρ_1, one may use the inverted sound speed of the sand ridge (c_1) as a constraint to repeat Step 1. This process using an exhaustive search is shown in Fig. 5. Inserting the estimated value for c_1 from the second step and inverted values for c_2 ρ_2, D_1, and D_2 from the first step into Eq. (5), we obtain $E_1(\mathbf{x})$ as a function of ρ_1 shown in Fig. 9(c). The inverted density of the sand ridge (ρ_1), corresponding to the minimum value of $E_1(\mathbf{x})$, is estimated to be 1648.5 kg/m^3. The first three rows of Table III summarize the search bounds and inverted results in the first two steps.

D. Uncertainty of inverted results caused by water column variability

The CSS signals studied in this paper were measured on September 4, 2006. The average SSP from all five ship board (R/V Knorr) CTD casts obtained during the CSS measurements on September 4, 2016 is used in the first two steps. The effect of water column sound speed variability on the parameters associated with the inversions employing mode shapes and group velocity dispersion curves is investigated by comparing the inverted parameters (c_1, c_2, ρ_1, ρ_2, D_1, and D_2) from each individual SSP. The mean and standard deviation of these results are listed in the fourth and fifth rows of Table III, respectively. The standard deviation represents the uncertainty due to water column SSP variation. The uncertainty of the parameters in the sand ridge (c_1, ρ_1, and D_2) is larger than that in the half-space basement (c_2 and ρ_2) and water depth (D_1).

V. GEOACOUSTIC INVERSION USING LONGITUDINAL HORIZONTAL COHERENCE

The similarity of the sound field can be described by the spatial coherence, which is sensitive to the seabed geoacoustic parameters in shallow water. Zhou *et al.*[19] have derived a mathematical model to calculate reverberation vertical coherence in shallow water and inverted the seabed sound speed and attenuation using measured reverberation cross-correlation coefficients. In this section, longitudinal horizontal coherence of the acoustic field measured by the L-shaped array is utilized to estimate the seabed sound attenuation (α_b).

A. The mathematical expression for the theoretical normalized longitudinal horizontal coherence in terms of normal modes

The spatial coherence is defined as the normalized cross correlation between the sound pressure received at two

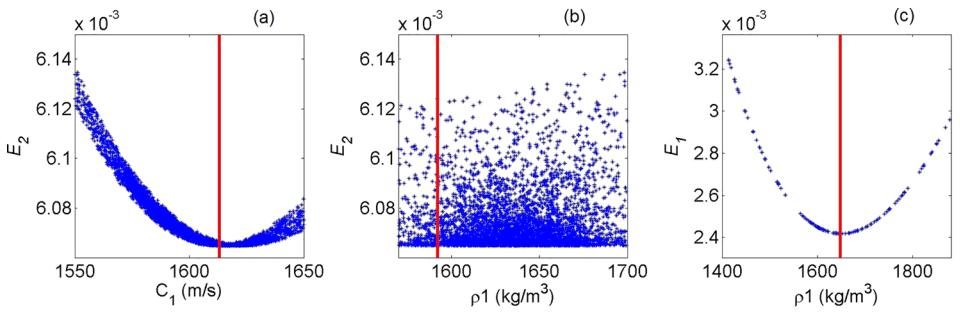

FIG. 9. (Color online) E_2 as a function of (a) sound speed in sand ridge and (b) density in sand ridge. E_1 as a function of (c) density in sand ridge after adding the constraint from (a), which is $C_1 = 1613.3\,(\text{m/s})$. The horizontal coordinate of the vertical line represents the inverted results.

TABLE III. Search bounds and inverted results.

Parameters	c_1(m/s)	c_2(m/s)	ρ_1(kg/m^3)	ρ_2(kg/m^3)	D_1 (m)	D_2 (m)
Bounds	[1530 1680]	[1680 1760]	[1300 2000]	[1700 2150]	[68 72]	[0 4]
Results from average SSP	1613.3	1730.0	1648.5	1844.0	70.8	1.37
Results from individual SSP	1638.3	1735.0	1665.2	1815.4	70.5	2.16
Standard deviation	29.7	5.3	257.1	75.1	0.97	0.95

spatially separated points. The expression of the longitudinal horizontal coherence is shown in Eq. (10),[33]

$$\gamma_{\mathrm{HL}}(z_s,z,r,\Delta L)=\frac{|\overline{p(z_s,z,r)p^*(z_s,z,r+\Delta L)}|}{\sqrt{\overline{|p(z_s,z,r)|^2}\,\overline{|p^*(z_s,z,r+\Delta L)|^2}}}, \tag{10}$$

where p is source pressure, r is range, z_s is SD, z is receiver depth, and ΔL is the horizontal separation between the pair of hydrophones. The asterisk indicates complex conjugate, and the overbar indicates an average over range.[34] The average over range means that the operator $(1/\Delta r)\int_0^{\Delta r}\cdots dr$ is applied as shown in Eq. (11),

$$\overline{|p(z_s,z,r)|^2}=\frac{1}{\Delta r}\int_0^{\Delta r}|p(z_s,z,r)|^2dr. \tag{11}$$

Using the expression for sound pressure generated by a harmonic point source ($k_n \gg \beta_n$)

$$p(z_s,z,r)=\frac{b}{\sqrt{r}}\sum_{n=1}^{M}\frac{\Psi_n(z_s)\Psi_n(z)\exp(ik_nr-\beta_nr)}{N_n\sqrt{k_n}}, \tag{12}$$

where b is a constant factor, the numerator in Eq. (10) then becomes

$$\begin{aligned}|\overline{p(z_s,z,r)p^*(z_s,z,r+\Delta L)}| &= \frac{|b|^2}{\sqrt{r(r+\Delta L)}}\left[\sum_{n=m}\overline{\Psi_n(z_s)^2}\,\overline{\Psi_n(z)\Psi_n(z)}\exp(-2\beta_nr-ik_n\Delta L)/\left(N_n^2k_n\right)\right.\\ &\left.+\sum_{n\neq m}\overline{\Psi_n(z_s)\Psi_n(z)\Psi_m^*(z_s)\Psi_m^*(z)}\exp\left(i(k_n-k_m)r-(\beta_n+\beta_m)r-ik_n\Delta L\right)/\left(N_nN_m\sqrt{k_nk_m}\right)\right],\end{aligned} \tag{13}$$

where β_n is the modal attenuation of the nth mode. The second term on the right side of Eq. (13) varies rapidly with range and becomes negligible with range averaging. Using Eqs. (12) and (13), the mathematical expressions in terms of normal modes for the theoretical normalized longitudinal horizontal coherence become

$$\gamma_{\mathrm{HL}}(z_s,z,\Delta L,r)=\frac{\left|\sum_n\overline{|\Psi_n(z_s)|^2}\,\overline{|\Psi_n(z)|^2}\exp(-2\beta_nr)\times\exp(-ik_n\Delta L)/\left(N_n^2k_n\right)\right|}{\sum_n\overline{|\Psi_n(z_s)|^2}\,\overline{|\Psi_n(z)|^2}\exp(-2\beta_nr)/\left(N_n^2k_n\right)}. \tag{14}$$

As a model for the square-average depth function ($\overline{\Psi_n(z)^2}$), the one proposed by Zhang and Jin[35] is selected where

$$\frac{\overline{\Psi_n(z)^2}}{N_n}=\frac{2k_n}{S_n\sqrt{k^2(z)F(z)+k^2(z)-k_n^2}}, \tag{15}$$

and S_n is the cycle distance of the nth mode, with

$$F(z)=0.875\left|\frac{1}{\pi f}\frac{dc(z)}{dz}\right|^{2/3} \tag{16}$$

and

$$k(z)=\frac{\omega}{c(z)}. \tag{17}$$

The normal-mode attenuation coefficient (β_n) can be solved from the expressions in Eq. (18),[20,28]

$$\begin{aligned}\beta_n=\frac{\omega}{k_nN_n}\left(\int_0^{D1}\frac{\alpha_0}{c_0(z)}\rho_0\Psi_n^2(z)dz+\int_{D1}^{D1+D2}\frac{\alpha_b}{c_1}\rho_1\Psi_n^2(z)dz\right.\\ \left.+\int_{D1+D2}^{\infty}\frac{\alpha_b}{c_2}\rho_2\Psi_n^2(z)dz\right),\end{aligned} \tag{18}$$

where α_0 is the sound attenuation in the water column obtained using the Thorp formula.[36] By substituting Eqs. (15), (16), (17), and (18) into Eq. (14), the theoretical normalized longitudinal horizontal correlation coefficients can be calculated.

B. The experimental longitudinal horizontal coherence measurements

The measured normalized longitudinal horizontal correlation coefficients can be obtained from

$$\hat{\gamma}_{\mathrm{HL}}(\Delta T,\tau)=\frac{\int_{t}^{t+\Delta T}\hat{p}_1(t)\hat{p}_2(t-\tau)dt}{\sqrt{\int_{t}^{t+\Delta T}\hat{p}_1^2(t)dt\int_{t}^{t+\Delta T}\hat{p}_2^2(t)dt}},\tag{19}$$

where τ is the time delay and ΔT is the integration time. $\hat{p}_1$ and $\hat{p}_2$ are sound pressures measured by two different hydrophones on the L-shaped array. The HLA component of SWAMI 32 was parallel to the direction of sound propagation, so the time delay for the longitudinal horizontal coherence is given by $\tau = \Delta L/c_0$.

An example explaining the data processing is provided in Fig. 10. The CSS time series received by channels 15 and 17 are shown in Figs. 10(a) and 10(b), respectively, of the SWAMI 32 HLA, when the CSS SD was 35 m and the source-receiver range was 10.81 km. The signals in Figs. 10(a) and 10(b) are filtered by the one-third octave bandpass filter with a center frequency of 50 Hz and an integration time of 1.6 s. The filtered signal and its envelope are shown as solid curves and dashed lines in Figs. 10(c) and 10(d), respectively. The time delay between channels 15 and 17 was 24 ms. The normalized cross correlation function evaluated by Eq. (19) and its upper/lower peak envelopes determined using spline interpolation over local maxima/minima are shown in Fig. 10(e). The longitudinal horizontal correlation coefficient for the two signals is 0.965.

The experimental spatial coherence is evaluated for the stated central frequency with a one-third octave bandwidth for SWAMI 32. The integration time for each frequency band is appropriately chosen so that the SNR of the modal arrivals is sufficient. The measured longitudinal horizontal coherence is obtained by averaging the data from the SWAMI 32 HLA, which has 20 longitudinal horizontal hydrophones. The moving average of the data from 190 hydrophone pairs is performed to smooth out the fluctuations. The horizontal separations of the 190 pairs of hydrophones can be calculated using the element spacing of SWAMI 32 shown in the top four rows of Table I. The array distortion due to a passage of tropical storm Ernesto is compensated for in this calculation. The experimental results at a range of 10.81 km for longitudinal horizontal correlation coefficient as a function of hydrophone separation (in units of wavelength λ) at three different frequencies (100, 200, and 400 Hz) are shown in Fig. 11. The coherence coefficient decreases with increasing hydrophone separation. The coherence coefficients of 100, 200, and 400 Hz fall below 0.8 at 3.2 λ, 4.0 λ, and 6.0 λ, respectively. This indicates the longitudinal horizontal coherence length in units of wavelength increases with frequency. This is because the bottom loss in general increases with frequency and the effective grazing angle of sound propagation decreases with increasing frequency. For a given distance, the smaller the effective grazing angle, the larger the longitudinal horizontal coherence length.[37]

C. Inversion scheme and results using longitudinal horizontal coherence

In this section, the inversion scheme and results based on longitudinal horizontal coherence are presented. This scheme is utilized to estimate the sea bottom attenuation as a function of frequency.

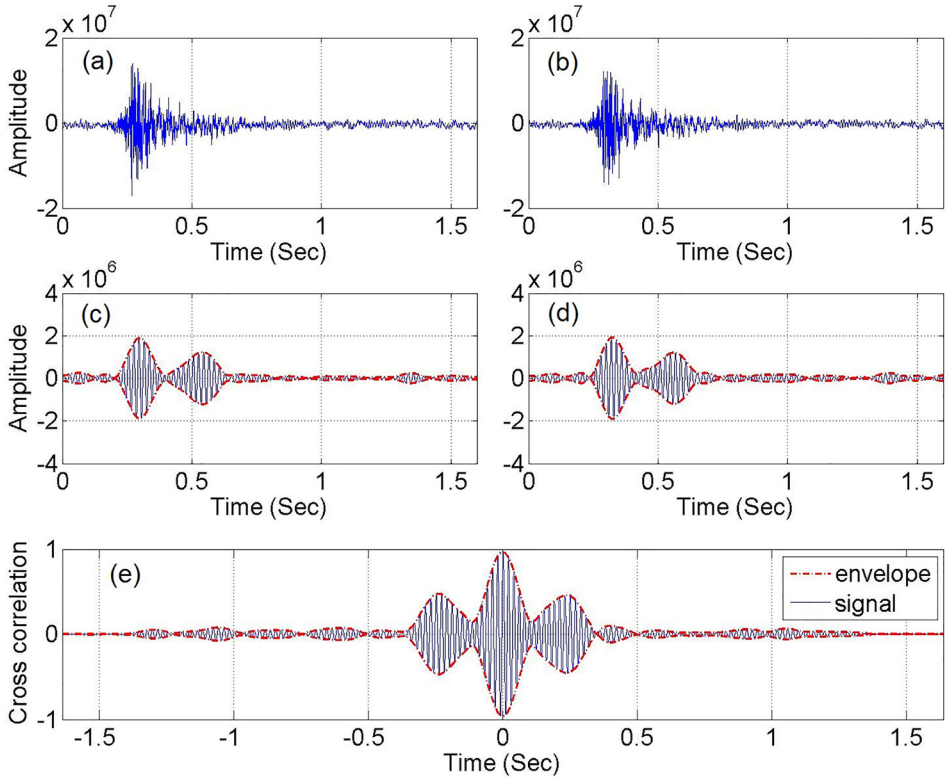

FIG. 10. (Color online) CSS signal received by SWAMI 32 at a range of 10.81 km. (a) and (b) Show the CSS time series received by channels 15 and 17, respectively. (c) and (d) The corresponding filtered signals and the envelope. (e) shows the normalized cross correlation function and its envelope.

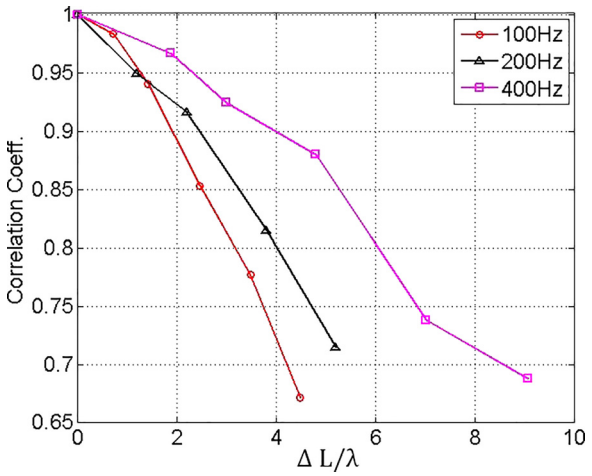

FIG. 11. (Color online) Longitudinal horizontal correlation coefficient as a function of hydrophone separation to wavelength ratio at three different frequencies: 100, 200, and 400 Hz.

The theoretical normalized longitudinal horizontal coherence (γ_{HL}) depends on the seabed attenuation (α_b), as shown in Eqs. (14) and (18). Therefore, α_b can be estimated by adjusting their input to KRAKEN such that the difference between modeled and measured longitudinal horizontal coherence is minimized. The objective function, Eq. (20), is used to calculate the data-model difference

$$E_{\mathrm{HL}}(\alpha_b) = \sqrt{\frac{1}{N_L}\sum_{j=1}^{N_L} |\hat{\gamma}_{\mathrm{HL}}(j) - \gamma_{\mathrm{HL}}(j)|^2}, \tag{20}$$

where N_L is the number of hydrophone pairs, $\hat{\gamma}_{\mathrm{HL}}(j)$ is the measured longitudinal horizontal correlation coefficient of the jth pair of hydrophones, and $\gamma_{\mathrm{HL}}(j)$ is the theoretical longitudinal horizontal correlation coefficient of the jth pair of hydrophones.

The estimation process is shown as Step 3 in Fig. 5. The KRAKEN calculated longitudinal horizontal correlation coefficient (γ_{HL}) as a function of seabed attenuation using the average measured water column sound speed profile, the inverted geoacoustic and geometrical parameters (c_1, ρ_1, c_2, ρ_2, D_1, and D_2) from the first and second objective functions. The experimental horizontal correlation coefficient ($\hat{\gamma}_{\mathrm{HL}}$) as a function of hydrophone separation to wavelength ratio, obtained at a distance of 10.81 km when SD = 35 m is used in the third objective function. An exhaustive search is utilized to invert the unknown seabed attenuation at different frequencies. The estimated value of E_{HL} as a function of seabed attenuation at (a) 50 Hz, (b) 100 Hz, (c) 200 Hz, (d) 250 Hz, (e) 400 Hz, and (f) 500 Hz is shown in Fig. 12. The inverted results associated with the minimum value of E_{HL} are shown as vertical lines in Fig. 12 and listed in the first two rows of Table IV. Using the power law fitting method, the inverted seabed attenuation can approximately be expressed by

$$\alpha_b = 0.26 f^{1.55}(\mathrm{dB/m}), \quad \text{in the 50 Hz–500 Hz band.} \tag{21}$$

D. Uncertainty of inverted seabed attenuation caused by water column variability

The average SSP from all five ship board (R/V Knorr) CTD casts on September 4, 2016 is used to calculate the longitudinal horizontal coherence and obtain the seabed attenuation expressed by Eq. (21). Uncertainty caused by water column variability is studied by comparing the inverted attenuation from each individual SSP. The mean and standard deviation of these results as a function of frequency are listed in the bottom two rows of Table IV, respectively. The standard deviation represents the uncertainty due to water column SSP variation. The small value of the standard

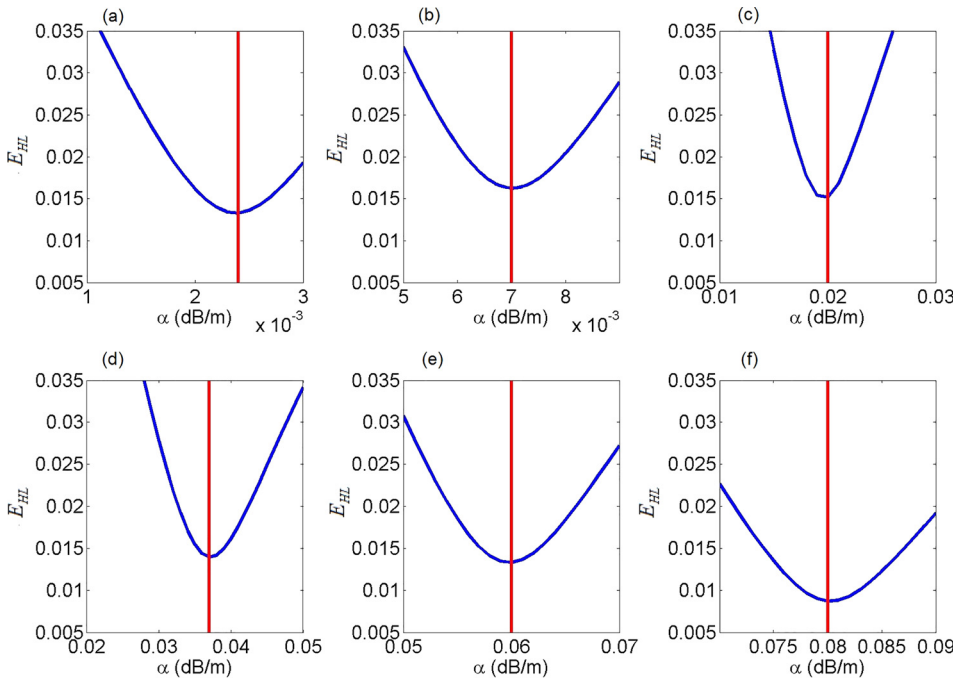

FIG. 12. (Color online) E_{HL} as a function of seabed attenuation at different frequencies: (a) 50 Hz, (b) 100 Hz, (c) 200 Hz, (d) 250 Hz, (e) 400 Hz, and (f) 500 Hz. The horizontal coordinate of the vertical line represents the inverted results.

TABLE IV. Inverted results using longitudinal horizontal coherence measurements.

f (Hz)	50	100	200	250	400	500
α_b(dB/m) from average SSP	0.0024	0.0070	0.020	0.037	0.060	0.080
α_b(dB/m) from individual SSP	0.0020	0.0060	0.020	0.035	0.058	0.079
Standard deviation (dB/m)	0.0003	0.0008	0.003	0.003	0.006	0.006

deviations indicate that the effect of the water column SSP variability on the inverted seabed attenuation is small for the data used in this paper.

VI. COMPARISON OF MODELED, MEASURED, AND OTHER RESULTS

In this section, the measured results of group velocity dispersion curves, mode shapes, and longitudinal horizontal coherence are compared with their theoretical predictions using the inverted seabed geoacoustic and geometrical parameters. In addition, the inverted sound speed and attenuation are also compared with the direct measurements at another location and other geoacoustic inversion results from SW06.

The simulated group velocity dispersion curves based on the inverted parameters are shown in Fig. 13 by dashed lines. The extracted data points used in the objective function are shown as triangles. It is noted that the simulation shows *the turn* of the modal Airy Phase. However, the energy of the CSS below the frequency corresponding to the minimum group velocity (Airy Phase) is weak for all the modes. Therefore one is unable to uniquely identify them. There are no data points in this region used in the objective function. The continuation of the data energy where the prediction shows an apparent turn, i.e., the energy below 5 Hz from 0.5 to 1.2 s, ~55 Hz around 1 s, and ~75 Hz from 1.1 to 1.2 s, appears to be due to the noise. In order to confirm this, we have included the data in this region for the inversion. However, no group velocity dispersion curves can be found to match both the data in this region and the ones shown as the triangles in Fig. 13. Therefore, only the extracted data points from the received CSS (i.e., triangles) are used in this inversion. The simulated curves show qualitative agreement with the extracted ones. The data-model comparison of mode shape at 25 Hz is shown in Fig. 8. The modeled shape based on the inverted parameters matches the data-derived one. The data-model comparison of longitudinal horizontal coherence at (a) 50 Hz, (b) 100 Hz, (c) 200 Hz, (d) 250 Hz, (e) 400 Hz, and (f) 500 Hz is shown in Fig. 14. The theoretical predictions are in qualitative agreement with the measured results.

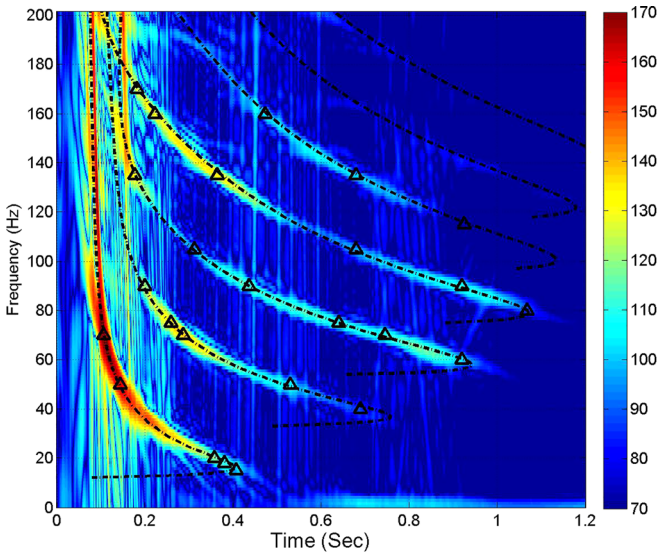

FIG. 13. (Color online) Data-model comparison of modal dispersion curves. The extracted data points used in the objective function are shown as triangles.

The inverted sound speed is compared with direct measurement results[27] and other inverted results from the acoustic measurements during SW06.[25,30,38,39] In Fig. 1, SB and RB are the source and receiver array locations reported by Bonnel and Chapman,[30] respectively. Huang *et al.*[38] used the short-range (1 km) sound propagation with the same receiver array located at RB. SP and RP denote the source and receiver positions used by Potty *et al.*,[39] respectively. The direct measurements of Yang *et al.*[27] were performed at the locations shown by diamonds. The acoustic signals in Knobles *et al.*[25] were measured by the same receiver arrays as the ones used in this paper. The sub-bottom chirp reflection profile of the seabed perpendicular to bathymetry isobaths (along A-RB) is also shown in Fig. 1. It is noted that these inversions in Refs. 30, 38, and 39 and the direct measurement in Ref. 27 are not on the sand ridge. Actually, they are in the 20-m thick outer shelf wedge, which were predominantly clay, with some interlayering of sand and silt.[26] In the direction from SWAMI 32 toward SWAMI 52, the depth of the outer shelf wedge decreases rapidly. About 2 km from SWAMI 32, the outer shelf wedge disappears entirely. Therefore, the two-layer sediment model (sand ridge over a half-space basement) is utilized in this paper whereas a different two-layer sediment model (outer shelf wedge over a half-space basement) was adopted in Refs. 30 and 38. Potty *et al.*[39] used the range-dependent sediment model containing outer shelf wedge and a half-space basement.

The estimated sound speeds in the top sediment layer (i.e., sand ridge in this paper and Ref. 25; outer shelf wedge in Refs. 30, 38, and 39) and the half-space basement are plotted in Figs. 15(a) and 15(b), respectively. The inverted results and their corresponding frequency ranges are indicated by straight lines. Their bottom models used in the inversion are also summarized in Table V. The outer shelf wedge had a sound speed of about 1560–1603 m/s at low frequency (see the fifth column of Table V), which is lower than that in the sand ridge layer.

In Fig. 16, the inverted seabed attenuation using the acoustic measurements from SW06 is plotted on the top of Fig. 13 from Ref. 20, which summarized the seabed attenuation in sandy sediments from more than 20 coastal regions around the world. The estimated attenuation in our paper falls within the bounds calculated by the Biot model with inputs A and B (see Table X BB fit by Zhou *et al.*[20]). The

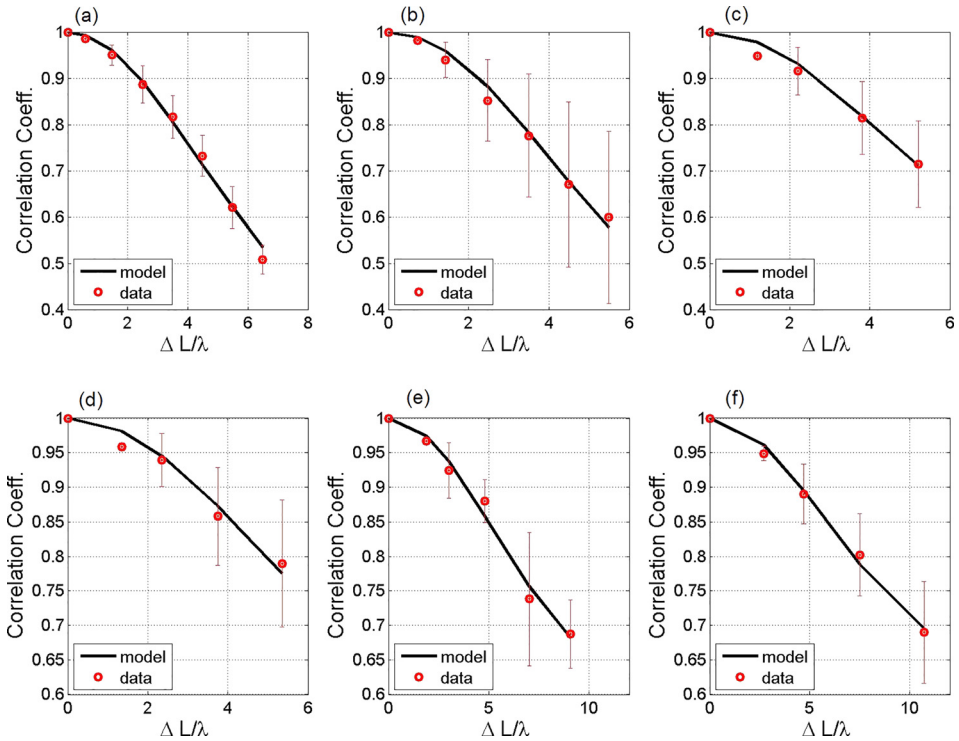

FIG. 14. (Color online) Data-model comparison of longitudinal horizontal coherence at different frequencies: (a) 50 Hz, (b) 100 Hz, (c) 200 Hz, (d) 250 Hz, (e) 400 Hz, and (f) 500 Hz. The error bars show the standard deviation of the correlation coefficients from different pairs of hydrophones.

frequency exponent (1.8 for 50 Hz–1000 Hz) by Zhou *et al.*[20] is the average results from more than 20 locations. The frequency exponent at different locations varies from 1.55 to 2. The estimated attenuation in this paper is comparable to the results by Knobles *et al.*[7] Both data sets are obtained using long-range acoustic measurements and exhibit nonlinear frequency dependence. The inverted attenuation in Ref. 7 can be expressed as $0.37f^{1.70}$ dB/m from 53 to 253 Hz. Similarly, the result in this paper is $0.32f^{1.65}$ dB/m in the frequency range of 50–250 Hz. The difference of the inverted attenuation from 400 to 500 Hz may be attributed to the fact that the inversion methods by Knobles *et al.*[7] and the current paper are very different. While the longitudinal horizontal coherence is utilized in this paper, Knobles *et al.*[7] applied TL measurements in the inversion scheme. Above 1000 Hz, the estimated seabed attenuation from short-range acoustic measurements[9,10] is smaller than the result from long-range acoustic measurements. One may ascribe this observation to the fact that long-range measurements involve a larger acoustic energy loss into the seabed by additional attenuation mechanisms, such as scattering by inhomogeneities within the sediment and roughness.

VII. SUMMARY AND CONCLUSION

Seabed geoacoustic parameter values at the SW06 experimental site are estimated by a three-objective inversion scheme, which involves the dispersion characteristics of

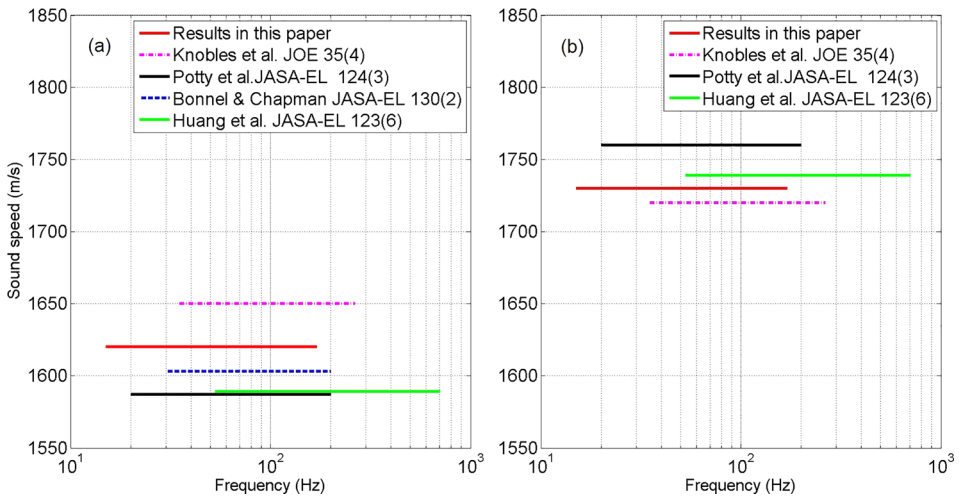

FIG. 15. (Color online) Summary of inverted sound speed during SW06. (a) Sound speed in the top sediment layer and (b) sound speed in the half-space basement.

TABLE V. Inverted sound speed from SW06.

				Sound Speed (m/s)	
	f (Hz)	Water Depth(m)	Sand ridge	Outer shelf wedge	Half-space bottom
Knobles (Ref. 25)	35–264	~70	1650	1580–1596	1720
Potty (Ref. 39)	20–200	65–110	N/A	1560–1600 (top 5 m)	1760
Bonnel (Ref. 30)	<200	~80	N/A	1603	2199
Huang (Ref. 38)	53–703	~80	N/A	1599.4	1739

broadband signals, mode shapes of the acoustic normal mode, and the longitudinal horizontal coherence of the received acoustic field. Over the frequency range of 15–170 Hz, the sound speed and density in the half-space basement are 1730.0 m/s and 1844.0 kg/m^3, respectively. The sound speed and density of the sand ridge are correlated to determine the modal arrival time difference. Using the second objective function defined by the mode shapes, the ambiguity of the sound speed and density in the sand ridge layer are removed. The resultant sound speed and density are estimated to be 1613.3 m/s and 1648.5 kg/m^3, respectively. The seabed sound attenuations are inferred by minimizing the difference between the theoretical and measured longitudinal horizontal coherence. The inverted seabed attenuation shows a nonlinear frequency dependence as $\alpha_b = 0.26f^{1.55}(\mathrm{dB/m})$ from 50 to 500 Hz or $\alpha_b = 0.32f^{1.65}(\mathrm{dB/m})$ from 50 to 250 Hz, where f is in kHz.

The SW06 experimental setup using two L-shaped arrays (i.e., one HLA is parallel and the other HLA is perpendicular to the direction of sound propagation) enabled us to obtain the group velocity dispersion curves, mode shapes, and longitudinal horizontal coherence in just one experiment. Using the similar experimental configuration, one is able to apply the three-objective inversion scheme for the seabed parameter inversion. One advantage of this approach is to remove the ambiguity among unknown parameters. The other advantage is that source level is not required in the seabed attenuation inversion, whereas it is needed in the TL approach by Knobles *et al.*[7] and maximum entropy approach by Knobles.[40] In a less well-known environment with internal wave activities, the water column variability may increase the uncertainty of the inverted parameters, thus more detailed water column measurements are preferable.

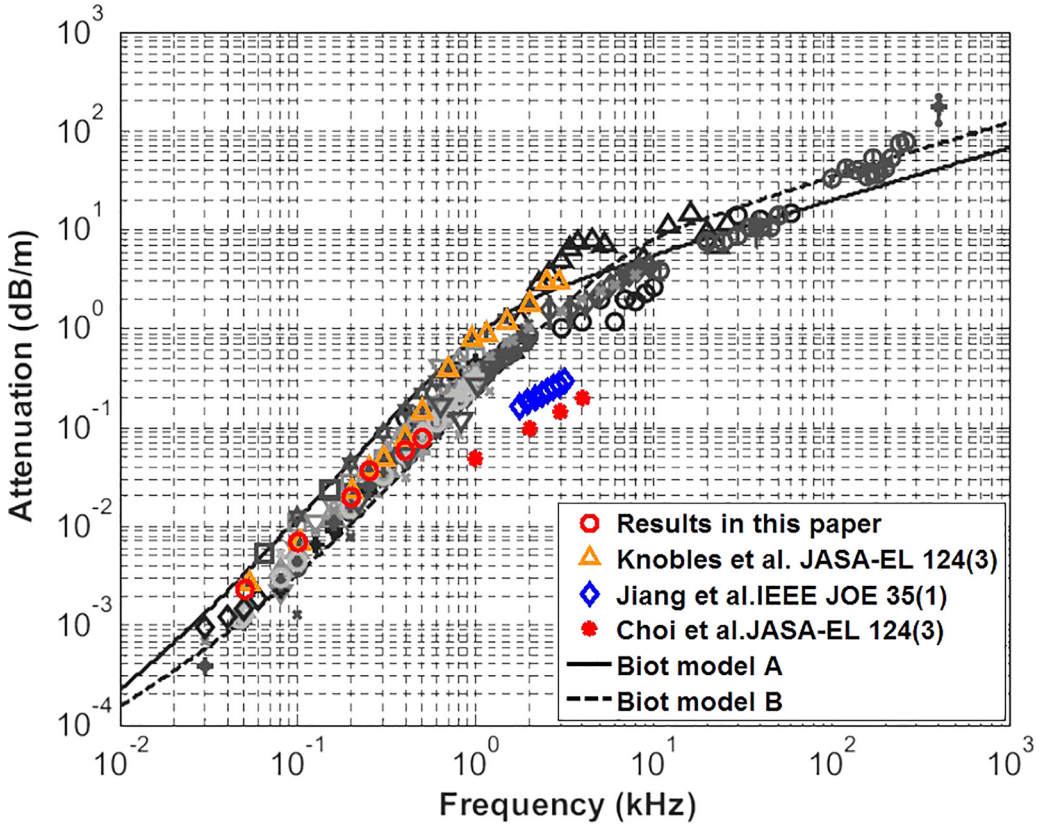

FIG. 16. (Color online) Inverted bottom attenuation in the SW06 area. The data points and curves in black and white are from Fig. 13 in Ref. 20.

ACKNOWLEDGMENTS

This work was sponsored by the Office of Naval Research [N00014-13-1-0306]. L.W. would like to express his great appreciation to Dr. Ji-Xun Zhou from Georgia Institute of Technology for his helpful discussions and comments. The authors want to thank Dr. Preston Wilson from the University of Texas at Austin for the CSS operation and the deployment of two SWAMI arrays during SW06. The authors also thank Dr. John Goff from the University of Texas at Austin for providing the CHIRP reflection survey data. The efforts of all the SW06 participants are gratefully acknowledged. Finally, the authors thank the associate editor and the two anonymous reviewers for their valuable comments and suggestions on the earlier version of this paper.

[1]E. L. Hamilton, "Geoacoustic modeling of the sea floor," J. Acoust. Soc. Am. **68**, 1313–1340 (1980).
[2]M. A. Biot, "Theory of propagation of elastic waves in a fluid-saturated porous solid," J. Acoust. Soc. Am. **28**, 168–191 (1956).
[3]M. A. Biot, "Generalized theory of acoustic propagation in porous dissipative media," J. Acoust. Soc. Am. **34**, 1254–1264 (1962).
[4]R. D. Stoll, "Marine sediment acoustics," J. Acoust. Soc. Am. **77**, 1789–1799 (1985).
[5]M. Badiey, A. H. Cheng, and Y. Mu, "From geology to geoacoustics—Evaluation of Biot-Stoll sound speed and attenuation for shallow water acoustics," J. Acoust. Soc. Am. **103**, 309–320 (1998).
[6]A. E. Newhall, T. F. Duda, J. D. Irish, K. von der Heydt, J. N. Kemp, S. A. Lerner, S. P. Liberatore, Y.-T. Lin, J. F. Lynch, A. R. Maffei, A. K. Morozov, A. Shmelev, C. J. Sellers, and W. E. Witzell, "Acoustic and oceanographic observations and configuration information for the WHOI moorings for the SW06 experiment," WHOI Technical Report No. WHOI-2007-04 (2007).
[7]D. P. Knobles, P. W. Wilson, J. A. Goff, and S. E. Cho, "Seabed acoustics of a sand ridge on the New Jersey continental shelf," J. Acoust. Soc. Am. **124**, EL151–EL156 (2008).
[8]Y. M. Jiang, N. R. Chapman, and P. Gerstoft, "Short range geoacoustic inversion with vertical line array," J. Acoust. Soc. Am. **124**, EL135–EL140 (2008).
[9]Y. M. Jiang and N. R. Chapman, "Measurement of low-frequency sound attenuation in marine sediment," IEEE J. Ocean. Eng. **35**, 70–78 (2010).
[10]J. W. Choi, P. H. Dahl, and J. A. Goff, "Observations of the R reflector and sediment interface reflection at the shallow water'06 central site," J. Acoust. Soc. Am. **124**, EL128–EL134 (2008).
[11]J. X. Zhou, "Normal mode measurements and remote sensing of seabottom sound velocity and attenuation in shallow water," J. Acoust. Soc. Am. **78**, 1003–1009 (1985).
[12]G. R. Potty, J. H. Miller, and J. F. Lynch, "Inversion for sediment geoacoustic properties at the New England Bight," J. Acoust. Soc. Am. **114**, 1874–1887 (2003).
[13]Z. L. Li and R. H. Zhang, "Geoacoustic inversion based on dispersion characteristic of normal modes in shallow water," Chin. Phys. Lett. **24**, 471–474 (2007).
[14]F. Ingenito, "Measurement of mode attenuation coefficients in shallow water," J. Acoust. Soc. Am. **53**, 858–863 (1973).
[15]C. T. Tindle, "Attenuation parameters from normal mode measurements," J. Acoust. Soc. Am. **71**, 1145–1148 (1982).
[16]J. X. Zhou, X. Z. Zhang, P. H. Rogers, and J. Jarzynski, "Geoacoustic parameters in a stratified sea bottom from shallow-water acoustic propagation," J. Acoust. Soc. Am. **82**, 2068–2074 (1987).
[17]P. Hursky, W. S. Hodgkiss, and W. A. Kuperman, "Matched field processing with data-derived modes," J. Acoust. Soc. Am. **109**, 1355–1366 (2001).
[18]L. Wan, J. X. Zhou, and P. H. Rogers, "Low-frequency sound speed and attenuation in sandy seabottom from long-range broadband acoustic measurements," J. Acoust. Soc. Am. **128**, 578–589 (2010).
[19]J. X. Zhou, X. Z. Zhang, P. H. Rogers, J. A. Simmen, P. H. Dahl, G. L. Jin, and Z. H. Peng, "Reverberation vertical coherence and sea-bottom geoacoustic inversion in shallow water," IEEE J. Ocean. Eng. **29**, 988–999 (2004).
[20]J. X. Zhou, X. Z. Zhang, and D. P. Knobles, "Low-frequency geoacoustic model for the effective properties of sandy seabottoms," J. Acoust. Soc. Am. **125**, 2847–2866 (2009).
[21]P. Gerstoft, "Inversion of seismo-acoustic data using genetic algorithms and a posteriori probability distributions," J. Acoust. Soc. Am. **95**, 770–782 (1994).
[22]C. Audet and J. E. Dennis, Jr., "Analysis of generalized pattern searches," SIAM J. Optimization **13**, 889–903 (2003).
[23]P. S., Wilson, J. L., Ellzey, and T. G. Muir, "Experimental investigation of the Combustive Sound Source," IEEE J. Ocean. Eng. **20**(4), 311–320 (1995).
[24]C. S. Fulthorpe and J. A. Austin, Jr., "Shallowly buried, enigmatic seismic stratigraphy on the New Jersey outer shelf: Evidence for the latest Pleistocene catastrophic erosion," Geology **32**, 1013–1016 (2004).
[25]D. P. Knobles, J. A. Goff, R. A. Koch, P. S. Wilson, and J. A. Shooter, "Effect of inhomogeneous sub-bottom layering on broadband acoustic propagation," IEEE J. Ocean. Eng. **35**, 732–743 (2010).
[26]J. A. Goff, B. J. Kraft, L. A. Mayer, S. G. Schock, C. K. Sommerfield, H. C. Olson, S. P. S. Gulick, and S. Nordfjord, "Seabed characterization on the New Jersey middle and outer shelf: Correlatability and spatial variability of seafloor sediment properties," Mar. Geol. **209**, 147–172 (2004).
[27]J. Yang, D. J. Tang, and K. L. Williams, "Direct measurement of sediment sound speed in Shallow Water'06," J. Acoust. Soc. Am. **124**, EL116–EL121 (2008).
[28]R. A. Koch, C. Penland, P. J. Vidmar, and K. E. Hawker, "On the calculation of normal mode group velocity and attenuation," J. Acoust. Soc. Am. **73**, 820–825 (1983).
[29]M. B. Porter, The KRAKEN Normal Mode Program, La Spezia, Italy (SACLANT Undersea Research Centre SM-245, 1991).
[30]J. Bonnel and N. R. Chapman, "Geoacoustic inversion in a dispersive waveguide using warping operators," J. Acoust. Soc. Am. **130**, EL101–EL107 (2011).
[31]P. Gerstoft, "Inversion of acoustic data using a combination of genetic algorithms and the Gauss-Newton approach," J. Acoust. Soc. Am. **97**, 2181–2191 (1995).
[32]T. B. Neilsen and E. K. Westwood, "Extraction of acoustic normal mode depth functions using vertical line array data," J. Acoust. Soc. Am. **111**, 748–756 (2002).
[33]Q. Wang and R. H. Zhang, "Sound spatial correlations in shallow water," J. Acoust. Soc. Am. **92**, 932–938 (1992).
[34]R. H. Zhang and Q. Wang, "Range and depth-averaged fields in ocean sound channels," J. Acoust. Soc. Am. **87**, 633–638 (1990).
[35]R. H. Zhang and G. L. Jin, "Normal-mode theory of the average reverberation intensity in shallow water," J. Sound Vib. **119**, 215–223 (1987).
[36]W. H. Thorp, "Analytic description of the low-frequency attenuation coefficient," J. Acoust. Soc. Am. **42**, 270 (1967).
[37]P. W. Smith, "Spatial coherence in multipath or multimodal channels," J. Acoust. Soc. Am. **60**, 305–310 (1976).
[38]C. F. Huang, P. Gerstoft, and W. S. Hodgkiss, "Effect of ocean sound speed uncertainty on matched-field geoacoustic inversion," J. Acoust. Soc. Am. **123**, EL162–EL168 (2008).
[39]G. R. Potty, J. H. Miller, P. S. Wilson, J. F. Lynch, and A. Newhall, "Geoacoustic inversion using combustive sound source signals," J. Acoust. Soc. Am. **124**, EL146–EL150 (2008).
[40]D. P. Knobles, "Maximum entropy inference of seabed attenuation parameters using ship radiated broadband noise," J. Acoust. Soc. Am. **138**, 3563–3575 (2015).